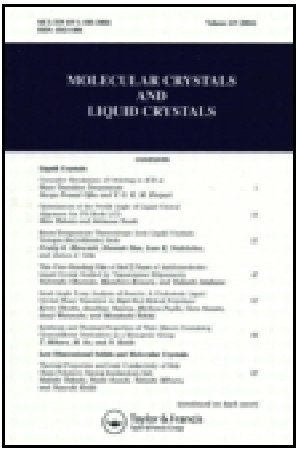

Molecular Crystals and Liquid Crystals Science and Technology. Section A. Molecular Crystals and Liquid Crystals
Publication details, including instructions for authors and subscription information:
http://www.tandfonline.com/loi/gmcl19

Heat Transport Through MBBA Due to Induced Electrohydrodynamic Motion

Rand R. Biggers [a] , Jeff W. Rish [b c] & Robert Fuller [c]

[a] Wright Laboratory, WL/MLPO Wright-Patterson AFB, OH, 45433-6533

[b] Coastal Systems Station, Code N1110, Panama City, FL, 32407-5000, Currently, WL/FIVCO, Tyndall AFB, FL, 32403-5323

[c] Currently, Medical Scholar, University of Illinois, Coastal Systems Station, Code N1110, Panama City, FL, 32407-5000

Version of record first published: 24 Sep 2006.

To cite this article: Rand R. Biggers , Jeff W. Rish & Robert Fuller (1993): Heat Transport Through MBBA Due to Induced Electrohydrodynamic Motion, Molecular Crystals and Liquid Crystals Science and Technology. Section A. Molecular Crystals and Liquid Crystals, 237:1, 351-376

To link to this article: http://dx.doi.org/10.1080/10587259308030149

Mol. Cryst. Liq. Cryst., 1993, Vol. 237, pp. 351–376
Reprints available directly from the publisher
Photocopying permitted by license only

Printed in the United States of America

Heat Transport Through MBBA Due to Induced Electrohydrodynamic Motion†

RAND R. BIGGERS,‡ JEFF W. RISH, III,§ and ROBERT FULLER||

‡Wright Laboratory, WL/MLPO Wright-Patterson AFB, OH 45433-6533; §Coastal Systems Station, Code N1110, Panama City, FL 32407-5000, Currently, WL/FIVCO, Tyndall AFB, FL 32403-5323; and ||Coastal Systems Station, Code N1110, Panama City, FL 32407-5000, Currently, Medical Scholar, University of Illinois

(Received January 3, 1993; in final form February 28, 1993)

Turbulent electrohydrodynamic (EHD) motion occurs in the liquid crystal MBBA [*p*-methoxybenzylidene *p*-(*n*-butyl)aniline] when subjected to large AC (sine wave) voltages. The onset of EHD motion substantially increases the transport of heat across a cell encapsulating the liquid crystal. This observed increase in heat transfer, or "heat valve effect," can be characterized by an "apparent" thermal conductivity k_a of the liquid crystal. The magnitude of the increase in k_a is a strong function of frequency, temperature, voltage, and the liquid-crystal phase. This k_a is actually a measure of the EHD motion within the cell. Structure in the k_a versus frequency curves indicates possible transitions in flow behavior. Internal heating also occurs within the liquid crystal and is shown to vary in strength with frequency, temperature, and applied voltage. Variations in the usual power factor normally associated with dielectric heating suggest that ionic double layers are formed below some critical frequency.

Keywords: apparent thermal conductivity, nematic liquid crystal, electrohydrodynamic motion, Joule heating, ionic double layer

1. INTRODUCTION

Thermotropic liquid crystals with small negative dielectric anisotropies, $\Delta\epsilon = \epsilon_{\parallel} - \epsilon_{\perp} < 0$, and positive electrical conductivity anisotropies, $\Delta\sigma = \sigma_{\parallel} - \sigma_{\perp} > 0$, exhibit electrohydrodynamic (EHD) motion and other convective instabilities under an external stress.[1,2] In this study, the liquid crystal MBBA is encapsulated in a thick (0.666 cm) cell and placed between 2 electrodes. The sample is heated from above to inhibit buoyancy induced flows, and small thermal gradients (about 2.9°C) are imposed across the sample to measure variations in the apparent thermal conductivity as a function of voltage, frequency, and temperature. In the absence of strong aligning fields and below a critical frequency ω_c, the voltage-induced instability will give rise to EHD motion.[1]

---

†The appearance of trade names in this document does not constitute endorsement by the Department of Defense; the Navy; or the Coastal Systems Station, Dahlgren Division, Naval Surface Warfare Center.

EHD motion in thermotropic liquid crystals is generally attributed to the Carr-Helfrich mechanism of space-charge separation and flow under the influence of applied voltage.[3,4] The natural parallel alignment of the long axis of the molecules in the nematic phase gives rise to a positive electrical conductivity anisotropy. When an electric field is applied this electrical anisotropy causes the impurity ions present in a liquid crystal to separate and form a space-charge dipole with a measurable component perpendicular to the applied electric field. The negative dielectric anisotropy of this liquid crystal supports formation of these dipoles by maintaining the general alignment of the liquid crystal axes perpendicular to the applied field. The space charge separation can initiate a buildup in a bend formation as shown in Figure 1. Above some voltage threshold, the buildup becomes unstable with respect to material flow parallel to the applied field E_z. In thin cells (10 to 200 μm thick) and at low applied fields (about 1000 V_{rms}/cm), this flow is laminar and results in well-structured flow patterns known as Williams domains. There is also an established dependence of the threshold voltage on frequency for the onset of the EHD motion and the formation of Williams domains. Plots of this threshold voltage as a function of frequency for thin samples[5] show a sudden dramatic increase (divergence) in the threshold voltage at a critical cutoff frequency, f_c. Williams domains do not occur at frequencies greater than f_c because the space-charge can no longer keep up (stay in phase) with the applied field. Although the relevance of this cutoff frequency for the turbulent flow in the "thick" sample of this study has yet to be established, this and other critical frequencies will be examined. The Williams domain cutoff frequency is given by

$$f_c = \frac{(\zeta^2 - 1)^{1/2}}{2\pi\tau} \tag{1}$$

where ζ^2 is the "Helfrich" parameter, characteristic of the material, and τ is the dielectric relaxation time.[5] The Helfrich parameter for MBBA ζ^2 is estimated to be 3.3 based on properties cited by Bodenschatz, Zimmermann, and Kramer.[6]

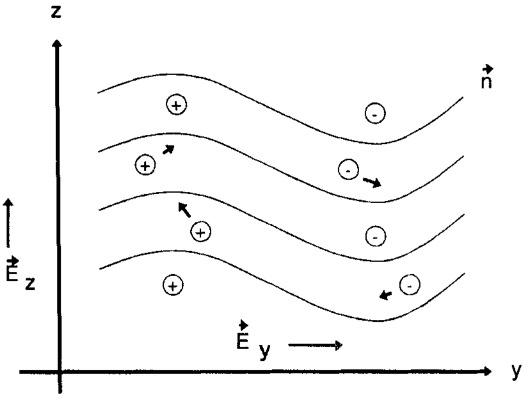

FIGURE 1 Simplified depiction of the net space charge separation and buildup in the region of a bend deformation due to the applied field E_z. The solid lines indicate the general direction of the alignment of the long axes of the liquid crystal molecules.

Values of ζ^2 ranging from 2 to 6 have been obtained from measured threshold voltages.[5,7] The larger values correspond to thicker samples. The associated dielectric relaxation time τ is normally defined as

$$\tau = \frac{\epsilon_0\epsilon_\parallel}{\sigma_\parallel} = \epsilon_0\epsilon_\parallel\rho_\parallel \tag{2}$$

It can also be expressed in terms of an RC time constant, i.e.,

$$\tau = R_pC \tag{3}$$

by considering the liquid crystal to be a parallel electrical network. In this relationship R_p is the parallel resistance and C the capacitance of the liquid crystal.

At frequencies below f_c, increasing the applied voltage results in a sequence of flow patterns that range from Williams domains to turbulence or "dynamic scattering."[8] This entire range of flows where $f < f_c$ is generally referred to as the "conduction regime," in which the charge separation and movement is in phase with the applied field. The director orientation remains static (for Williams domains), and the general alignment of the liquid crystal has been called anomalous.[7] A second regime, the dielectric regime, occurs for frequencies greater than f_c where the instabilities are not Williams domains, but show more complicated optical patterns. Here the motion is expected to be more oscillatory and in the direction of the applied field.[9] Below the critical threshold voltage of domain formation in the dielectric regime, the applied field tends to align the liquid crystal according to its dielectric anisotropy, e.g., normal alignment.[7] For liquid crystals with $\Delta\epsilon < 0$, as is the case in this study, the long axis would be aligned perpendicular to the applied field and the thermal conductivity becomes a minimum. Pieranski, Brochard, and Guyon[10] used a comparison technique to measure thermal conductivities of MBBA, both perpendicular and parallel to the long molecular axis under non-EHD (static) conditions. They determined that $k_\perp = 3.05 \pm 0.25 \times 10^{-4}$ cal/cm-sec-°C and $k_\parallel = 5 \pm 0.25 \times 10^{-4}$ cal/cm-sec-°C.

Optically observed EHD motions from Williams domains[11] to turbulence[12] occur in thick cells of MBBA (0.2 to 0.7 cm) at root-mean-square (rms) voltages ranging from 10 to 6000 volts. This EHD motion in thick cells was first associated with extremely large "apparent" thermal conductivities by Carr and various co-workers.[13,14] Very little other work concerning this phenomenon in thick samples has been published. However, Biggers, Rish, and Henderson[15] reported measurements of enhanced apparent thermal conductivities, k_a, in thick (0.666 cm) MBBA cells at high AC voltages. These measurements showed that the apparent thermal conductivity is a strong function of frequency as well as voltage. An internal heating effect was also detected and found to show voltage and frequency dependencies. This internal heating is suggestive of dielectric heating as seen in dielectric liquids under large AC potentials.[16] In this case, the heating mechanism is primarily Joule heating.

The subject of this paper is a study of heat transport due to EHD motion in thick (0.666 cm) MBBA cells. The apparent thermal conductivity k_a and the heat

Q_d generated by Joule heating are measured for MBBA as functions of the applied voltage and frequency. The effect of temperature and phase dependence are also examined. The MBBA studied was purchased from Aldrich Chemical, lot #HM-08114JK. The nematic-to-isotropic transition temperature, $T_{N/I}$ was measured as 40.5°C at a heating rate of 0.5°C/min on a differential scanning calorimeter (DSC) before beginning the experiments.

2. EXPERIMENTAL APPARATUS

The apparatus used to make the thermal measurements is of the cut bar type and shown in Figure 2(a). This device contains two 1.588 cm diameter by 20 cm long columns mounted in aluminum blocks. Each block can be maintained at near-constant temperature by constant temperature circulators. The upper column is heated while the lower column is cooled to provide the temperature gradient across the sample. The columns are composed of a very low thermal conductivity (54.7×10^{-4} cal/cm-sec-°C) alumina silicate material to provide a large temperature drop per length of column when the ends are maintained at different temperatures.

Copper-constantan thermocouples are attached to the columns and the aluminum blocks at predetermined positions for temperature monitoring and temperature control. The minimum thermocouple spacing is near the junctions of the columns and the sample. Temperature gradients are used to determine the heat flux in and out of the sample region assuming that no other heat sources or sinks are present. Line noise was reduced by connecting the low (constantan) side of the thermocouples to guard and the copper shield to ground. A significant amount of line noise existed at 60 Hz and its harmonics, but most was removed by the primary data acquisition unit, a Hewlett Packard, HP-44701A, integrating voltmeter.

The sample and sample holder, as illustrated in Figure 2(b), consists of MBBA encapsulated in a 0.652 cm long PTFE (Teflon) cylinder sandwiched between two 0.056 cm thick by 2.223 cm diameter sapphire disks. The Teflon cylinder is flared at the top and bottom and joined to the sapphire disks by Torr Seal epoxy. The inner diameter of the Teflon cylinder is the same as that of the columns, 1.588 cm. The walls of the Teflon cylinder were thinned to about 0.071 cm to minimize longitudinal heat transfer. Three very shallow parallel grooves in the cylinder wall allow precise attachment of thermocouples to monitor the sample temperature profile. Two additional thermocouples were attached to the sapphire disks, one to each disk on the side facing the MBBA. These 2 thermocouples are used to determine the temperature drop across the sample.

The region connecting the end of each column to the faces of the sample consists of a sapphire disk and a copper electrode (0.018 cm by 1.9 cm in diameter) which is adjacent to the sapphire disk of the sample cell. The electric field between the two electrodes is parallel to the direction of measured heat transfer. All of the rigid or semi-rigid materials are joined together by a layer (about 0.0094 cm) of Omega thermal grease which has a published thermal conductivity of 55×10^{-4} cal/cm-sec-°C. The sapphire disks are essentially inert and have a high thermal conductivity (800×10^{-4} cal/cm-sec-°C) relative to the sample and columns and

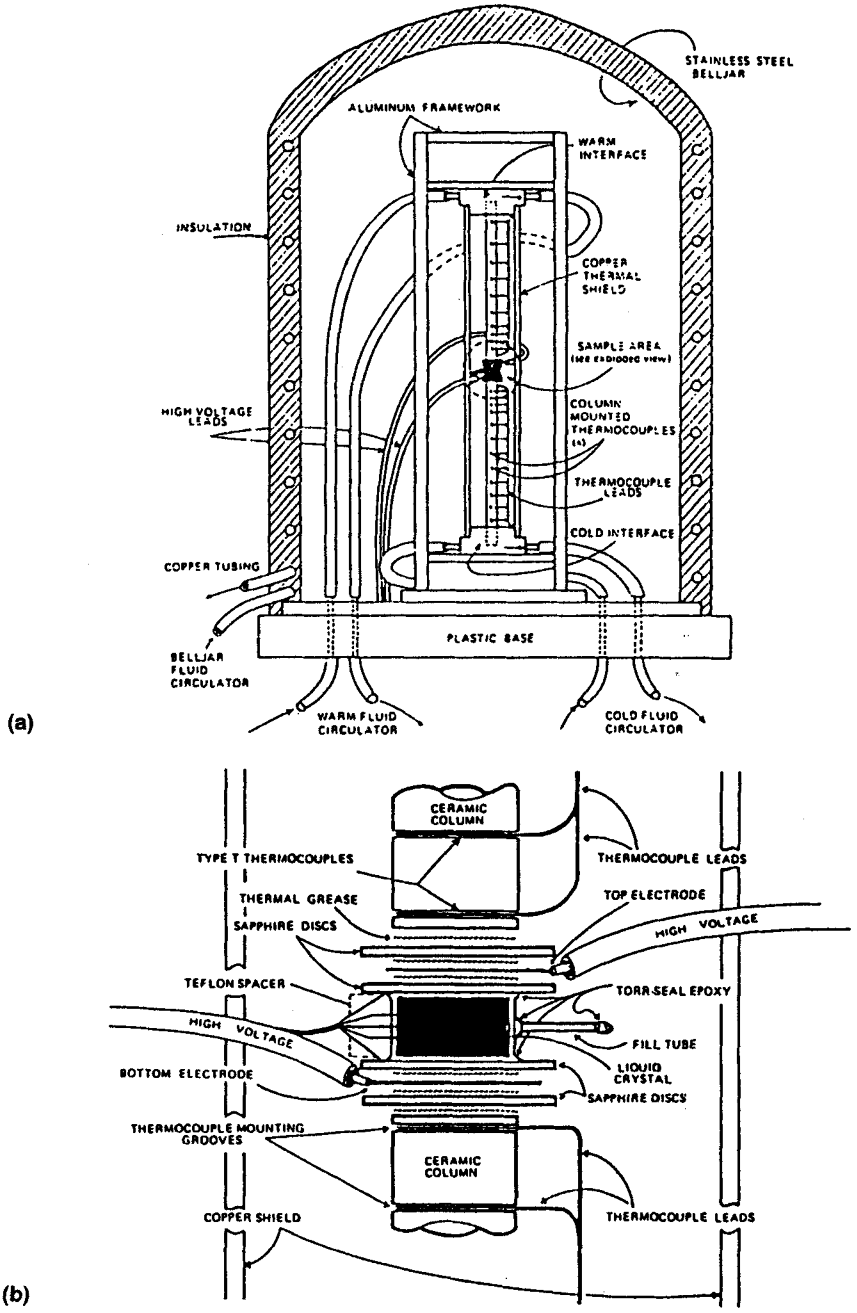

FIGURE 2 Experimental apparatus (a) Bell-jar, base-plate, framework, columns, and fluid connections; (b) exploded view of the liquid crystal sample area.

a very large electrical resistivity (9×10^{11} Ohm-cm). These disks serve to minimize arcing between the electrodes at large AC fields in addition to forming part of the sample cell.

A tubular copper shield surrounds the columns and the sample. The main purpose of the shield is to reduce the thermal interaction between the external environment and the sample. The shield is 7.62 cm in diameter, constructed in three sections, and made of two layers of 0.018 cm thick sheet. The top and bottom sections are attached to the corresponding constant temperature interfaces. Each section has ports for high-voltage and thermocouple wiring. One thermistor is mounted on the exterior of the shield opposite the sample. Temperature measurements made with this thermister and the thermocouple at the sample midpoint provide a measure of the thermal coupling between the shield and the sample. Convection heat loss or gain in the area between the copper shield, the columns, and the interfaces is minimized by heating the sample from above and by maintaining the copper shield at nearly the same temperature as the opposing section of the columns or sample.

The entire column assembly is enclosed in a stainless steel bell-jar. Copper tubing, 0.95 cm in diameter, has been wound concentrically around the exterior of the bell-jar and connected to a third constant temperature circulator. The bell jar is covered with a layer of thermal insulation, and a thermistor attached to the inside surface of the bell-jar is used to monitor the bell-jar temperature. The temperature-controlled bell-jar minimizes the environmental coupling between the sample and room temperature oscillations. The bell-jar sits on a 7.62 cm thick low thermal conductivity (5.25×10^{-4} cal/cm-sec-°C) Ultem baseplate that is 76.2 cm by 76.2 cm. The area where the bell-jar contacts the baseplate has been smoothed and flattened such that a good vacuum seal can be formed between the baseplate and the bell-jar. Vacuum fittings in the baseplate provide connections for the electrical wiring and fluid tubing entering the bell-jar.

AC voltage is supplied to the electrodes by a high-voltage system in which the frequency is manually set by a voltage controlled oscillator. The oscillator signal is multiplied by a variable 10 VDC signal from a computer to control the voltage amplitude. The resultant signal is amplified by a bridge amplifier and fed to a step-up transformer. A second step-up transformer (a neon light 1 to 125 transformer) outputs a sine wave at up to 15 $\mathrm{kV_{rms}}$ dependent on the frequency. Frequencies can be selected from 13 to 900 Hz. The experiment can be run manually or entirely under computer control.

Calibration

In order to assure good measurements, it was necessary to have accurate values for the thermal conductivity k_c of the columns. This was determined by two methods. The first method involved a series of calibration runs using known solid samples between the columns. Two of the samples were plastics of very low thermal conductivity, and the third was stainless steel with a relatively high thermal conductivity. The thermal contact resistance between the columns and sample was also unknown, so data from two different samples were used to solve for k_c and the thermal contact resistance coefficient h_c. The coefficient of thermal contact resistance is defined as[17]

$$h_c = \frac{q}{A_c \Delta T} \tag{4}$$

where q is the heat transferred through the thermal contact area A_c over which there is a temperature drop of ΔT. The values for k_c and h_c based on data from all three samples were respectively 55.3×10^{-4} cal/cm-sec-°C and 4.9×10^{-2} cal/cm^2-sec-°C. This value for h_c was primarily determined from the stainless steel data, which were much more sensitive to h_c than was the data for the low thermal conductivity samples.

A set of independent measurements on the alumina silicate column material was performed by the National Institute of Standards and Technology (NIST).[18] These results showed the thermal conductivity of the columns to be $k_c = 54.47 \times 10^{-4}$ cal/cm-sec-°C. There is excellent agreement (1.5% relative) between the above calculated value and NBS value. The manufacturer's published value of 25.8×10^{-4} cal/cm-sec-°C differs from the measured values by more than a factor two.

Sample Preparation

A Teflon tube was placed in the middle of the sample holder wall to permit filling with MBBA, and the holder was filled with MBBA in a vacuum oven held at 50°C. A vacuum was held on the sample components overnight to remove trapped water and gases. The next day the vacuum oven was slowly repressurized with dry nitrogen. This method permitted filling the sample holder without trapped air or bubbles. The sample cell and fill-tube were then removed from the oven and the sample cell placed on a hot plate maintained at about 50°C. The fill-tube was then cut off about 2.5 cm from the sample cell and the end covered with Torr Seal. There was some cooling of the sample and contraction of the MBBA resulting in some of the Torr Seal being sucked down into the fill-tube. A small bubble of air was trapped in the fill-tube between the MBBA and the Torr Seal. After allowing the sealant to cure for 24 hours the sample cell was placed in between the columns and electrodes.

3. PROCEDURE

All "apparent" thermal conductivity measurements made during this series of experiments assume that the temperature drop across the sample and the heat fluxes on either side of the sample are known. The heat fluxes are determined from the temperature profile along the 12 cm of each column immediately adjacent to the sample. The thermocouple density along each column increases as the column-sample interface is approached. The thermocouples attached to the sample provided the temperature drop across the sample as well as an exterior temperature profile of the sample. The sign of the temperature difference, $\Delta T_E = \Delta T_{\text{smp}} -$

ΔT_{sh} between the thermocouple reading on the PTFE cylinder at the middle of the sample (T_{smp}) and the thermistor on the copper shield (T_{sh}) indicates whether the sample was being heated or cooled by the shield. A positive temperature difference represents a heat loss; whereas, a negative value represents a heat gain.

All circulators were maintained at their set-point temperatures to within ±0.02°C. The actual temperatures at the constant temperature interfaces differed slightly (and were less stable) from the circulator set-point temperatures due to fluid heat loss or gain in the hoses. The temperatures used in all calculations were measured by thermocouples well away from the interfaces where the thermal fluctuations were found to be insufficient to jeopardize the repeatability of the experiments.

All pertinent experimental parameters were entered in to the computer for the automated runs. The computer would set all the circulators to the desired temperatures and monitor the temperatures of the interfaces and the bell-jar, before data acquisition was initiated. The circulator temperatures were incremented at half hour intervals to bring the interfaces and the bell-jar closer to the desired temperatures. Generally within three hours the bell-jar and the interfaces were regulated to ±0.1°C of the desired temperature and stable to within ±0.02°C during a 20 second temperature sampling period. The four thermocouples on the columns nearest the sample region were also monitored for stability. A standard deviation of ±0.03°C or less in these thermocouples was assumed to imply thermal equilibrium, and the data acquisition was initiated.

The desired voltage for a preset frequency was set by the computer at the beginning of a 9-minute interval. At the end of the 9-minute interval, the temperatures of all the thermocouples and thermistors in the system were read, and the next desired voltage was set. Approximately 1.3 minutes were required for the integrating voltmeter to take 25 readings from each of the 30 temperature sensors. Each of the 25 readings was an integral average of 590 readings.

Data Reduction

The apparent thermal conductivity k_a can be obtained from the data by assuming one-dimensional heat flow and solving the steady-state heat equation with internal heat generation

$$k_a \frac{d^2T(y)}{dy^2} + \dot{q} = 0 \tag{5}$$

where $\dot{q}$ is a uniform volumetric heat source. Under this set of assumptions, conservation of energy dictates that the rate of heat transfer from the heated column to the sample q_u is given by

$$\begin{aligned} q_u &= -k_c A_c \left(\frac{dT}{dy}\right)_c \bigg|_{y=y_u} \\ &= -k_a A_{lc} \left(\frac{dT}{dy}\right)_{lc} \bigg|_{y=y_u} - k_{\text{cyl}} A_{\text{cyl}} \left(\frac{dT}{dy}\right)_{\text{cyl}} \bigg|_{y=y_u} \end{aligned} \tag{6}$$

and the rate of heat transfer from the sample to the cooled column q_1 is

$$\begin{aligned} q_1 &= -k_c A_c \left(\frac{dT}{dy}\right)_c \Bigg|_{y=y_l} \\ &= -k_a A_{lc} \left(\frac{dT}{dy}\right)_{lc} \Bigg|_{y=y_l} - k_{\text{cyl}} A_{\text{cyl}} \left(\frac{dT}{dy}\right)_{\text{cyl}} \Bigg|_{y=y_l} \end{aligned} \tag{7}$$

The quantities k_c and k_{cyl} are the thermal conductivities of the columns and the Teflon cylinder respectively, and k_a is the apparent thermal conductivity of the liquid crystal. A_c, A_{cyl}, and A_{lc} are the corresponding cross-sectional areas normal to the flow of heat. Expressions for k_a and $\dot{q}$ are then derived by integrating Equation (5), applying the above matching conditions, and specifying the temperatures at the sample-column interfaces. The results are

$$k_a = -\frac{1}{2A_{lc}}(q_u + q_l)\frac{y_u - y_l}{T_u - T_l} - k_{\text{cyl}}\left(\frac{A_{\text{cyl}}}{A_{lc}}\right) \tag{8}$$

and

$$\dot{q} = \frac{q_u - q_l}{A_{lc}(y_u - y_l)} \tag{9}$$

where y_u and y_l are the coordinates of the top and bottom (heated and cooled) surfaces of the sample cells, and T_u and T_l are the measured temperatures at these locations. The heat transfer rates q_u and q_l were determined by the temperature profiles measured on the columns immediately adjacent to the sample. A third order fit was used to determine the temperature gradients.

Equations (8) and (9) are approximations in which heat losses/gains through the cell wall are ignored. Environmental energy exchange, viscous/thermal effects associated with the induced EHD motion within the cell, and temporal effects all contribute to the temperature profile data, and the net effect is reflected in the calculated value of the volumetric heat generation term. The losses and other extraneous effects are on the order of

$$Q_{\text{env}} = \dot{q}_{\text{actual}} V_{lc} - k_c A_c \left[\left(\frac{dT}{dy}\right)_{y_u} - \left(\frac{dT}{dy}\right)_{y_l}\right] \tag{10}$$

where $\dot{q}_{\text{actual}}$ is the "true" volumetric heat source, and V_{lc} is the volume of liquid crystal within the cell.

It can be shown that the presence of a positive heat source (heat generation) within the sample will tend to reduce the slope of the temperature profile on the heated side of the sample while increasing the slope on the cooled side of the sample. This phenomena is illustrated in Figure 3(a). The data in this case indicates

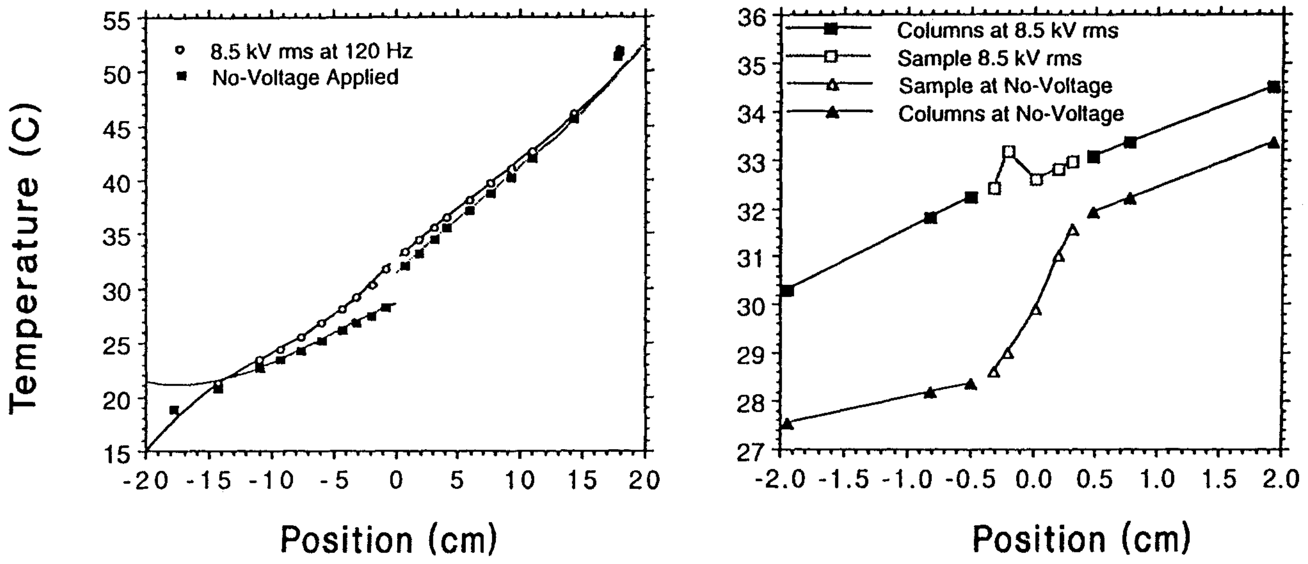

FIGURE 3 Temperature verus position for no-field conditions and after application of an applied voltage of 8.5 kV$_{rms}$ at 120 Hz: (a) Column temperatures as a function of vertical position relative to the center of the sample; (b) blow-up of the sample region including nearby column thermocouples. A peak was always present in the temperature profile on the sample when a voltage was applied.

a net heat source of about 38 mW within the sample. Other measurements, to be discussed later, suggest a temperature dependence of the magnitude of the internal heating through the temperature/phase dependence of the viscosity of MBBA.

The total heating rate in milliwatts at any voltage and frequency can be determined by

$$Q_d = (\dot{q}_f - \dot{q}_0)A_{lc}\Delta y_{lc} \tag{11}$$

where $\Delta y_{lc} = y_u - y_l$ is the thickness of the MBBA over which the heating takes place, $\dot{q}_f$ is the volumetric heat source in the presence of an AC field, and $\dot{q}_0$ is a volumetric "heat source" determined for "no-voltage" conditions. The "no-voltage" value is, in reality, a measure of the environmental energy exchange cited earlier. Baseline "no-voltage" measurements are taken at the start, in the middle, and at the end of a sample run to correct the calculated values for Q_d when the baseline value drifts during an experiment. It is important to obtain the best possible value for Q_d, since errors in Q_d show up as errors in other derived properties.

4. EXPERIMENTAL RESULTS

Several sets of experiments were run to evaluate the thermal transport capabilities of the encapsulated liquid crystal. The first series of experiments were run with the top constant temperature interface set at 58°C and the bottom at 13°C. This provided a 2.7°C temperature drop across the sample cell with the sample midpoint temperature about 30°C. The voltage applied across the sample was varied from 0 to 9.5 kV_{rms} depending on the output of the high voltage transformer at the selected frequency. The frequencies ranged from DC to 720 Hz. Another set of experiments were run in which the sample temperature was varied to provide measurements in the crystalline, near-crystalline, near-isotropic and isotropic phases. Unless stated otherwise, all reported voltages were corrected for the voltage drops across the two sapphire disks according to

$$V_{lc} = \frac{V\Delta y_{lc}}{2\left(\dfrac{\epsilon_a}{\epsilon_{\text{sapp}}}\right)\Delta y_{\text{sapp}} + \Delta y_{lc}} \tag{12}$$

where ϵ_a the apparent dielectric constant of the liquid crystal (taken to be 5), ϵ_{sapp} is the dielectric constant of the sapphire disks (taken to be 11), Δy_{sapp} is the thickness of the sapphire disk, and V is the voltage applied between the 2 electrodes.

Two examples of measured temperature profiles are shown in Figure 3. The measured temperature profiles were typically characterized by pronounced end effects near the heating and cooling interfaces. These nonlinear end effects decreased to insignificant levels outside of the vicinity of the constant-temperature aluminum blocks—especially in no-voltage cases with the bell-jar temperature set near the sample midpoint temperature T_{smp}. A comparison of the temperature gradient (*dT*/*dy*) along the columns at the column-sample interfaces show the magnitude of the slope of the temperature profile on the cooled side to be less than on the heated side. This is consistent with the bell-jar temperature at 24°C, about 5°C lower than T_{smp}, and indicates a slight heat loss from the sample. The shield midpoint temperature in this case is 1.5°C lower than T_{smp}. When the bell-jar temperature was set to the sample midpoint temperature, the magnitudes of the slopes on either side of the sample were approximately equal. Initial calculations show that the sample exchanges approximately 10 mW of power with the environment per °C difference between the sample midpoint temperature and shield temperature.

Figure 3 also shows the temperature profile that occurred when an 8.5 kV_{rms} potential was applied across the sample at a frequency of 120 Hz. This temperature profile displays the same type of nonlinearities near the heating and cooling interfaces as were observed in the no-voltage case. However, there are also distinct nonlinearities near the column-sample interface that result in large differences in the slopes of the temperature profiles on the heated and cooled sides of the sample. The sample midpoint temperature increased by 2.7°C above the value obtained for the no-field case, while the temperature drop across the sample decreased from 2.91°C to 0.53°C. The shapes of the temperature profiles near the sample are consistent with heat generation within the sample.

Figure 4 shows the variation of the apparent thermal conductivity k_a of the MBBA sample with voltage for a select number of frequencies and a sample midpoint temperature of approximately 30°C. The maximum magnitude of k_a, 78×10^{-4} cal/cm-sec-°C, occurs at 129 Hz and 8.6 kV_{rms} while the no-voltage minimum is about 9.6×10^{-4} cal/cm-sec-°C. Nearly equal minimum magnitudes of k_a per kV were measured at 24 Hz and at 720 Hz. The shape of the curves suggest a V^2 dependence which is confirmed by the plots of k_a versus V^2_{rms}. Plots for 24, 40, 70, 129, and 300 Hz are shown in Figure 5.

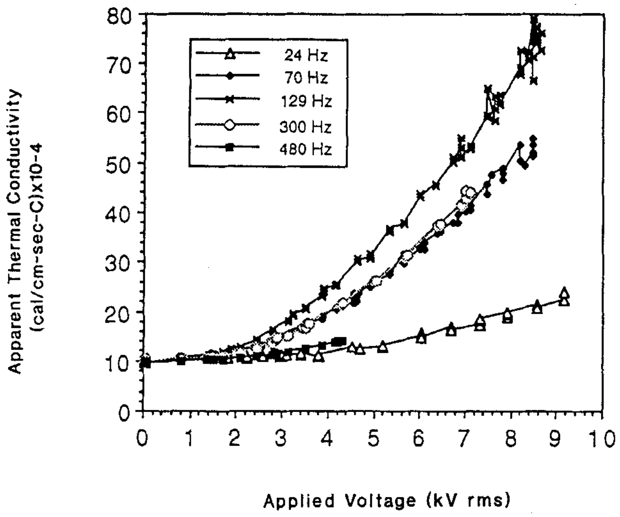

FIGURE 4 Variation of the apparent thermal conductivity k_a with applied voltage at selected frequencies.

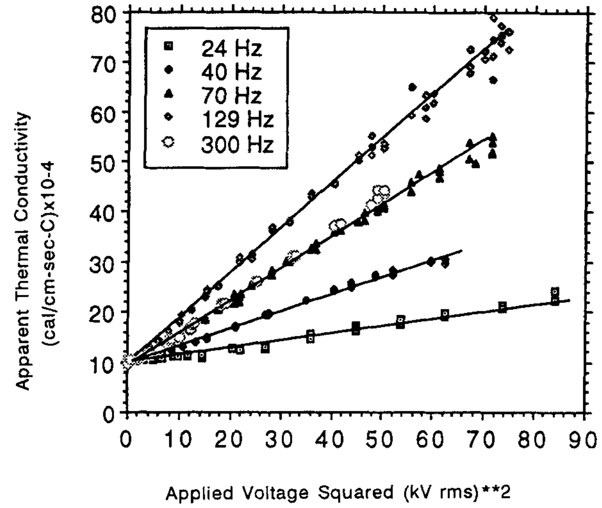

FIGURE 5 Variation of the apparent thermal conductivity k_a with the square of the applied voltage at selected frequencies.

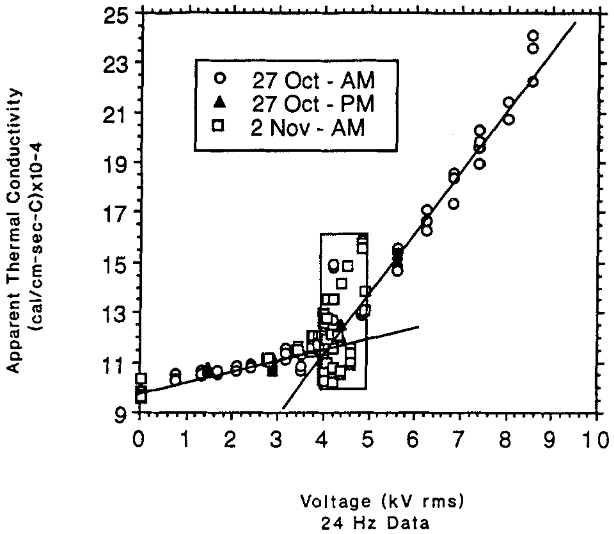

FIGURE 6 Variation of the apparent thermal conductivity k_a with the rms voltage at 24 Hz. The change in slope in the vicinity of 4 kV_{rms} may be indicative of a transition to turbulent flow.

At the lowest utilized frequency, 24.4 Hz, the general behavior of k_a in the midvoltage range was distinctly different than at all other frequencies. Figure 6 shows a large amount of scatter in the k_a values at voltages between 3.8 and 5.0 kV_{rms}. Three different data sets are overlaid in this figure encompassing measurements made more than a week apart. Straight lines can be drawn through the data from 0.7 to 3.8 kV_{rms} and from 5.0 to 9.1 kV_{rms}. The scatter that occurs near the intersection of these straight lines may indicate a transition from one type of flow to another as the voltage is increased, possibly similar to the flow patterns seen in thin cells in Reference 8. However, there is also a possibility that this scatter is a result of a non-isolated noise source.

The behavior of k_a as a function of frequency at a constant potential of 4.2 kV_{rms} is shown in Figure 7 with the sample near 30°C. The apparent thermal conductivity curve shows a sharp increase from the minimum value to a maximum of 28×10^{-4} cal/cm-sec-°C at 129 Hz and then an almost exponential decrease to a second minimum of 10.5×10^{-4} cal/cm-sec-°C at 720 Hz. For a sample midpoint temperature of 14.5°C, the peak in k_a is near 60 Hz and of much reduced magnitude with a peak value of 12.5×10^{-4} cal/cm-sec-°C. This decrease in magnitude and frequency is due in part to the substantial increase in the mean viscosity at 14.5°C.[22]

The dip below the no-voltage thermal conductivity k_0 (the dashed line) at 280 Hz and above is suggestive of a transition from the conduction to the dielectric regime. The overall alignment is believed to change from anomalous to normal, where a normal alignment is consistent with a minimum k when perpendicular to the applied field. This type of transition is usually associated with a cutoff frequency f_c, the frequency at which the motion of space charges is no longer in phase with the applied field. The occurrence of a lower cutoff frequency for the cooler sample is consistent with increased viscosity (and resistivity) at lower temperatures, i.e., $f_c \propto 1/\rho$ from Equations (1) and (2). Calculations of a cutoff frequency f_c at $T_{smp} = 30°C$ using Equations (1), (2), and (3) gives an f_c of 100 Hz if ϵ_1 is taken to be 4.72, $R_p = 1.9 \times 10^9$ Ohms, $C = 1.3 \times 10^{-12}$ Farads, and $\zeta^2 = 3.3$. At 14.5°C, f_c is calculated to be 27 Hz with $R_p = 7.0 \times 10^9$ Ohms. If 280 Hz is considered to be the cutoff frequency, then the calculated value at 14.5°C is about a factor of

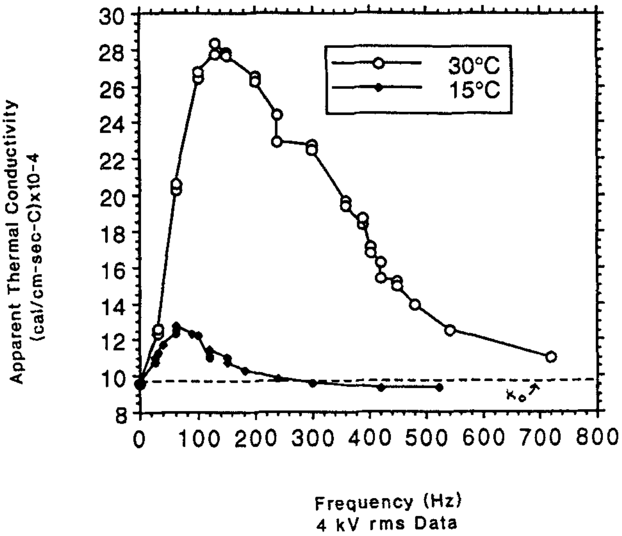

FIGURE 7 Variation of the apparent thermal conductivity k_a with frequency at 4.0 kV_{rms} for 15°C and 30°C. The dashed line represents the no-voltage thermal conductivity k_0 of 9.6×10^{-4} cal/cm-sec-°C. The point at which the 15°C curve drops below k_0 indicates a transition to the dielectric regime where MBBA would tend to align normal to the field and a heat transfer minimum would be expected.

10 too small. Increasing f_c at 30°C by a factor of 10 gives 1000 Hz which is well above the highest frequency at which k_a was measured.

There are several unknowns which limit our ability to establish direct correlations between the cutoff frequency as given by Equation (1) and the frequency at which k_a becomes less than k_0—the assumed entrance into the dielectric regime. The first unknown is an accurate value for R_p. The R_p used may be too large. Measurements of the onset of Williams domains in a thin sample (135 μm) of the same lot material as used in a prior investigation[15] indicated a cutoff frequency of about 410 Hz at 25°C.[19] Even if reduced values of R_p are used, sizeable discrepancies still remain in the observed and calculated cutoff frequencies. The most likely explanation for these discrepancies is that the relationship given by Equation (1) is not suitable for calculating the cutoff frequencies for turbulent flows in thick cells.

Figure 8 shows plots of the total internal heat generation Q_d versus k_a for 5 selected frequencies. Except for the 720 Hz and 480 Hz curves, which include only 0 to 3.9 kV$_{\text{rms}}$ potentials, the data is for applied voltages that range from 0 to 6.6 kV$_{\text{rms}}$. The increase of the slopes of the curves with increasing frequency is associated with the efficiency at which heat is transferred across the cell. An inverse relationship is indicated between the magnitude of the slope and the heat transfer efficiency. For the steep slopes at high frequencies, internal heating is dominant, and can overcome any benefit obtained by the slight increase in the apparent thermal conductivity.

Bell-jar temperature control was not available at the time most of the data used to determine the heat source was taken, and temperature control of the lab environment was limited. The heat source Q_d was found to be much more sensitive

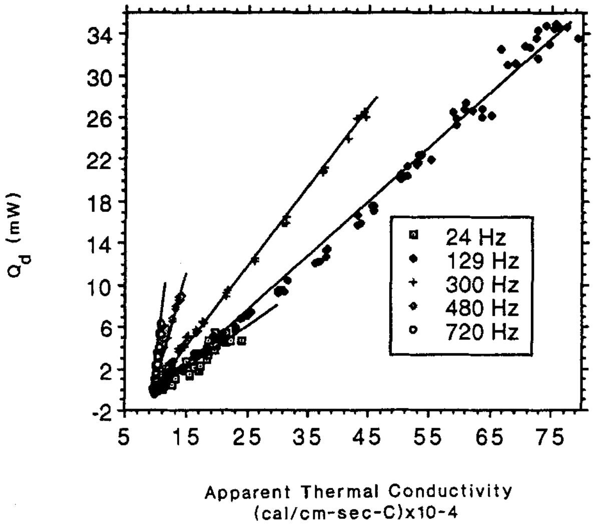

FIGURE 8 Relationship between the internal heating Q_d and the apparent thermal conductivity k_a at selected frequencies. The slopes tend to increase with increasing frequency. All curves include data taken at voltages between 0 and 6.6 kV$_{\text{rms}}$ except the data at 480 and 720 Hz where the maximum voltage was 3.9 kV$_{\text{rms}}$.

to the external temperature fluctuations than was the apparent thermal conductivity, k_a.

Influence of Ionic Shielding

The liquid crystal sample cell is essentially a capacitor and can be represented by a parallel RC circuit as shown in Figure 9.[20] In this representation, C is the pure capacitance of the cell, R_p is the parallel resistance associated with the internal heating, and C_{el} is the effective capacitance of the ionic double layer which shields the bulk of the sample from the full applied voltage below some critical frequency, f_d. Joule heating is expected to vary linearly with the square of the applied voltage and this relationship is verified by the data shown in Figure 10. The slopes of the Q_d versus V^2 curves at frequencies above 90 Hz (129, 300, and 480 Hz shown) are nearly identical except for some minimal scatter. The inverse of these slopes are the apparent parallel resistance R_p. The frequency dependence of R_p starts to disappear at frequencies above 100 Hz, and it appears to approach a constant value. The internal heating is also expected to be essentially independent of frequency at constant voltages however this is not seen in Figures 10 and 11. The effect of the screening of the ionic double layer below f_d, can easily be seen in Figures 11, 12, and 13. The internal heating sharply rises with increasing fequency up to about 100 Hz after which it remains relatively constant. Because the shield midpoint temperature could not be maintained at the sample midpoint temperature the magnitude of the calculated internal heating is not exact.

Based on the circuit model shown in Figure 9, the parallel resistance R_p of the RC system should be constant. It should therefore be possible to solve for R_p by setting V_{rms}^2/R_p (where V is corrected for the voltage drop across the sapphire disks) equal to Q_d. The resistivity of the material ρ, which can be related to the parallel resistance via $\rho = R_p A_{lc}/\Delta y$, is plotted as a function of frequency along with an extrapolation of an apparent average dielectric constant in Figure 12. Above 90–100 Hz, the resistivity becomes relatively constant at 5.7×10^9 Ohms. Since ρ for the material is presumed to be a constant, the deviation in the calculated value of

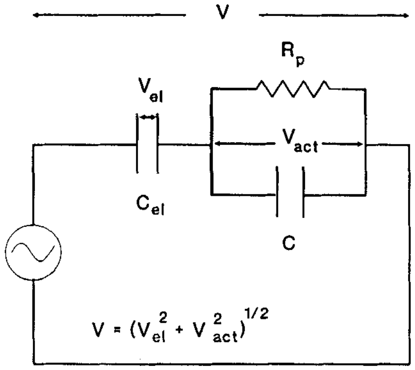

FIGURE 9 Simple circuit representation of the encapsulated liquid crystal MBBA between electrodes with an applied voltage as proposed by Sprokel.[20] C_{el} is the effective capacitance of the ionic double layer, C the pure capacitance of the MBBA, and R_p the parallel resistance of the MBBA.

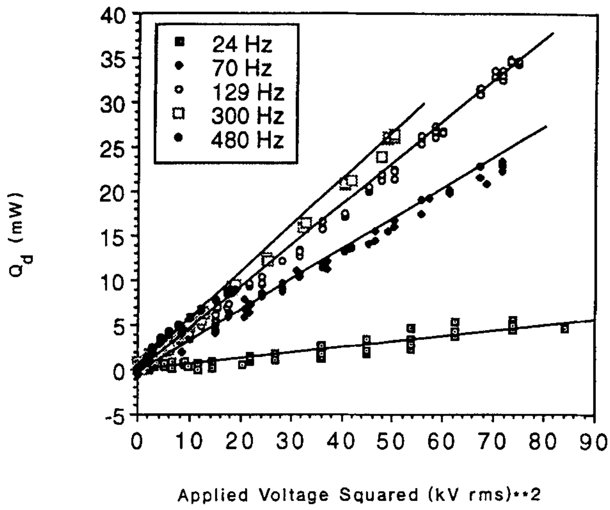

FIGURE 10 Linear variation of the internal heating Q_d with the square of the voltage for selected frequencies. The inverse of the slope of each curve on this plot represents an effective value of R_p at that frequency. The slopes reach a constant plateau at frequencies beyond 100 Hz for MBBA.

ρ below 100 Hz reinforces the assumption of a frequency dependent ionic shielding of the type postulated by Sprokel that effectively reduces the voltage drop across the liquid crystal.

A power factor (*PF*), which is the percentage of applied power converted to heat, can also be calculated as a function of frequency according to the following equation:

$$PF = \frac{Z_p}{R_p} \tag{13}$$

where Z_p is the complex impedance of the MBBA cell and is given by

$$Z_p = \frac{\chi_c R_p}{(\chi_c^2 + R_p^2)^{1/2}} \tag{14}$$

The capacitance reactance χ_c is given by

$$\chi_c = \frac{1}{\omega C} \tag{15}$$

The capacitance C was calculated to be about 1.3×10^{-12} Farads using an assumed value of 5.0 for the average dielectric constant. This value of ϵ_a is consistent with the calculated average value of 4.9 obtained by assuming $\epsilon_{\parallel} = 5.25$ and $\epsilon_{\perp} = 4.72$. However, if the capacitance of the system is calculated from R_p and the measured power factor PF_m, the apparent average dielectric constant ϵ_a will exhibit

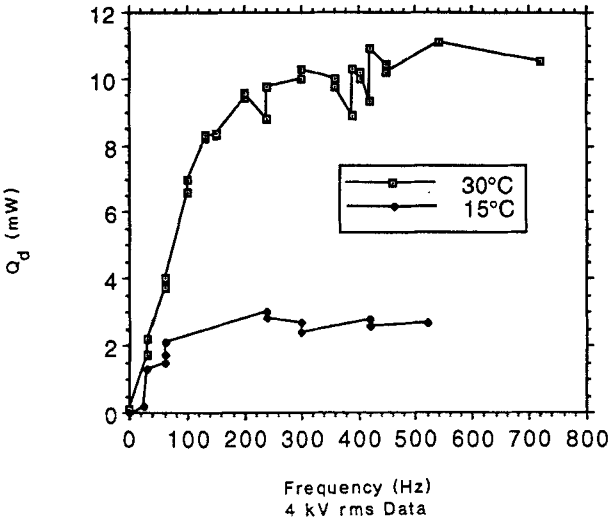

FIGURE 11 Variation of the internal heating (power dissipated) Q_d with frequency for a voltage of 4.2 kV_{rms} and at temperatures of 15°C and 30°C. The curves tend to flatten out at higher frequencies. The shape of the curves suggests a voltage shielding which disappears beyond some critical frequency.

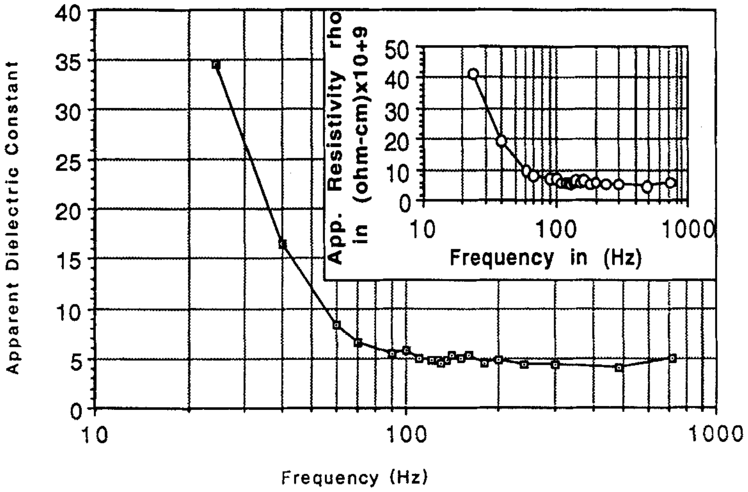

FIGURE 12 Variation of the apparent dielectric constant ϵ_a and the apparent resistivity ρ with frequency.

a divergent behavior at low frequencies. Figure 12 shows that such a divergence occurs in the current sample for frequencies below 90 Hz.

The expression for the apparent dielectric constant ϵ_a based on the measured power factor is given by

$$\epsilon_a = \frac{d(1 - PF_m^2)^{1/2}}{\epsilon_0 A_{lc} \omega R_p PF_m} \tag{16}$$

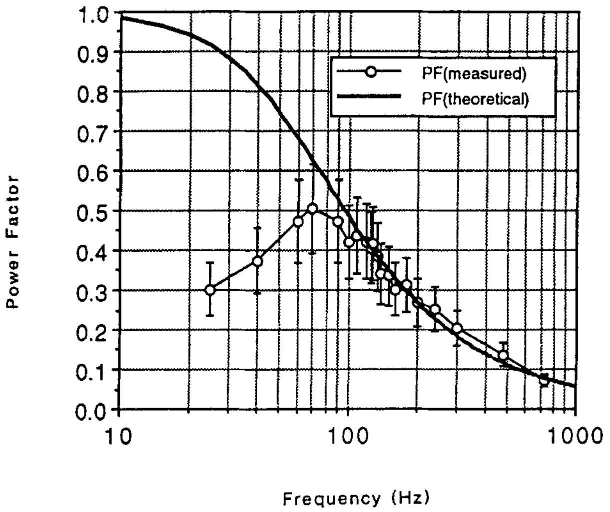

FIGURE 13 Comparison of the measured and theoretical power factor of the MBBA samples as a function of frequency. The circles represent power factors calculated using the measured values of R_p, and the error bars assume a 10% error in R_p and a 6% error in χ_c from the uncertainty in ϵ. The theoretical power factor was calculated with R_p of $1.9 \times 10^9\ \Omega$.

where $d = 0.666$ cm, $A = 1.967$ cm^2, and $\epsilon_0 = 8.85 \times 10^{-14}$ F/cm. It becomes approximately 5 at frequencies above 90 Hz, because that was the value used in the calculation of PF in Equation (13).

Figure 13 shows the variation of PF with frequency calculated using the R_ps from the ρs plotted in Figure 12. Overlaid on Figure 13 is the curve of the PF calculated using a constant value of 5.7×10^9 Ohm-cm from the constant region of Figure 12. The measured values of PF agree quite well with the theoretical PF curve above 100 Hz. The behavior in the region at and below 100 Hz is believed to be due to the ionic shielding. The error bars have been calculated from the scatter in R_p above 90 Hz of ±10% coupled with an assumed error in ϵ of ±6% to give ±22% using Equations (13), (14), and (15).

According to Sprokel,[20] the ionic shielding is due to the build-up of a double layer of ions near the capacitor plates. The effect of the double layer can be treated as if it were another capacitance C_{el} in series with the liquid crystal. The magnitudes of C_{el} and the percent shielding from the applied voltage can be calculated using Equations (17) through (19) below:

$$C_{el} = \frac{-C - \left[C^2 - \left(1 - \frac{V_{\mathrm{rms}}^2}{Q_d R_p}\right)\left(C^2 + \frac{1}{R_p^2 \omega^2}\right)\right]^{1/2}}{\left(1 - \frac{V_{\mathrm{rms}}^2}{Q_d R_p}\right)} \tag{17}$$

where V is the voltage across the entire sample cell as set by the computer

$$\text{percent shielding} = \left(1 - \frac{V_{\mathrm{act}}}{V}\right) \times 100 \tag{18}$$

with

$$V_{\text{act}} = \frac{V\omega C_{el}R_p}{[1 + \omega^2 R_p^2 (C + C_{el})^2]^{1/2}} \tag{19}$$

and where V_{act}, the effective voltage, is the actual voltage seen by the bulk of the liquid crystal. The Debye length associated with the shielding ionic double layer can be found using:

$$L_d = \left(\frac{\epsilon_0 k_b T\rho\mu e}{4\pi e^2}\right)^{1/2} \tag{20}$$

where ρ is the apparent resistivity, e is the electronic charge, and μ is the estimated ionic mobility (2×10^{-5} cm^2/sec-V at 30°C) calculated from the diffusivity coefficients from Reference 9. The maximum Debye length must be less than 1 μm. The calculated L_d values ranged from 0.14 μm at 24 Hz to 0.05 μm at 100 Hz and above. If ρ is halved then the L_ds will be decreased by a factor of $\sqrt{2}$. These calculations indicate that if anything ρ is too small and could be larger, the opposite indication of the previous f_c calculations. Calculated values of power factor, apparent dielectric constant, capacitance of the ionic double layer, percent shielding, and Debye lengths are reported in Table I.

The ionic shielding percentages listed in Table I can be used to extrapolate the apparent thermal conductivities that the sample would have if there were no ionic

TABLE I

Measured power factors and parameters associated with the ionic double layer

f (Hz)	PF (Measured)	ϵ_a	C_{el} (μf)	Shielding (%)	L_d (μm)
24.4	0.30	34	1.8	0.85	0.14
40.	0.37	16	2.4	0.70	0.09
60.	0.47	8	5.7	0.39	0.07
70.	0.50	7	11.1	0.23	0.06
90.	0.47	6	31.0	0.10	0.05
100.	0.42	6	21.0	0.13	0.05
110.	0.44	5	>> C	~ 0	<0.05
126.	0.41	5	>> C	~ 0	<0.05
129.	0.42	5	>> C	~ 0	<0.05
135.	0.38	5	>> C	~ 0	<0.05
140.	0.34	5	>> C	~ 0	<0.05
150.	0.33	5	>> C	~ 0	<0.05
160.	0.30	5	>> C	~ 0	<0.05
180.	0.31	5	>> C	~ 0	<0.05
200.	0.27	5	>> C	~ 0	<0.05
240.	0.25	4	>> C	~ 0	<0.05
300.	0.20	4	>> C	~ 0	<0.05
480.	0.14	4	>> C	~ 0	<0.05
720.	0.07	5	>> C	~ 0	<0.05

shielding at low frequencies. These results are shown in Figure 14 where the idealized values of the apparent thermal conductivity k_a are plotted as a function of frequency along with the measured k_a data at a voltage of 4 kV_{rms}. They were obtained by assuming that k_a varies linearly with the square of the voltage as implied by Figure 5, and then using the shielding percentages to extrapolate the ideal values from the measured data. The results show that k_a decreases with increasing frequency, and the prominent peak is removed. Figure 14 also more clearly connects the behavior of the heat transport phenomena (which is directly coupled to the EHD-induced flow velocities) with optically observed EHD parameters, such as the size and density of tube vortices, from Reference 12. In those observations, the vortex width at a fixed voltage increased with increasing frequency. The optical data also indicated that, at a fixed frequency, vortex widths decreased while particle velocities increased with increasing voltage. The implication is that small flow cells at the lowest possible operating frequency would tend to produce the highest flow velocities, and thus, the highest apparent thermal conductivities.

Measurement Results from the Solid to the Isotropic Phases

The heat transport due to EHD motion of the liquid crystal was examined at a number of different temperatures ranging from about 6°C to about 45°C. Differential scanning calorimeter (DSC) measurements indicated the pre-encapsulated MBBA had a nematic-to-isotropic (N/I) transition temperature $T_{N/I}$ at approximately 41°C and a crystalline-to-nematic (K/N) transition temperature $T_{K/N}$ at approximately 21°C. During the sample evaluation period, $T_{N/I}$ dropped to about 39°C while $T_{K/N}$ dropped to less than 14°C over the four month period of evaluations.

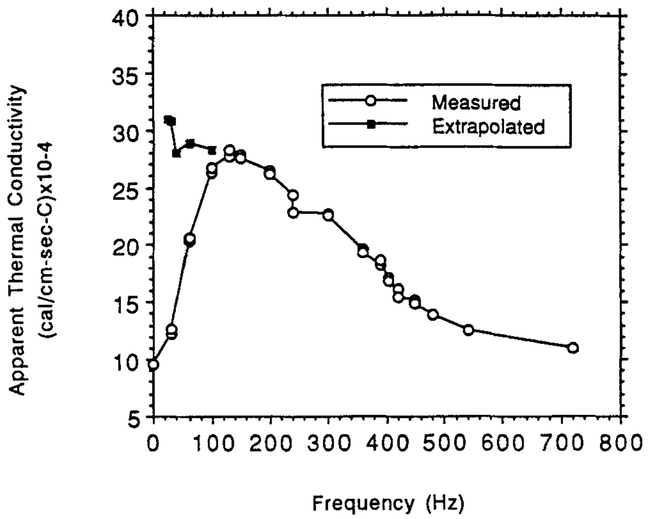

FIGURE 14 Variation of the apparent thermal conductivity k_a with frequency at a temperature of 30°C and voltage of 4 kV_{rms}. The squares represent idealized values of k_a extrapolated by subtracting the effect of ionic shielding from the measured data. The ionic shielding essentially disappears at frequencies above 100 Hz for this sample.

The reductions in transition temperatures are consistent with hydrolysis of the liquid crystal MBBA which is a Schiff's base material.[21] The sample was carefully sealed in an air-tight container to try to eliminate hydrolysis effects. However, upon termination of these experiments, it was discovered that the sample holder had lost its air-tight seal. A very small bubble, less than 0.5 mm in diameter, was found in the MBBA. The bubble was probably caused by thermal expansion and contraction of the liquid crystal when the sample was subjected to large changes in temperature. A new encapsulation method was developed which maintains sample cell integrity while allowing for significant volume changes with temperature.

Several experients were later run to examine the effect of a bubble in the sample. The conclusion was that unless the bubble was about 1.5 mm or larger in diameter, there were no obvious effects. For a 2.5 mm bubble, the temperature profile of the sample showed a ΔT of 2.7°C between the top of the sample and the end of the column. In the no-voltage condition, the end position of the heating column was also at a higher temperature than under the same conditions for a non-bubble sample.

In Figure 15, the variation of the k_a with applied potential at 120 Hz is shown for four sample midpoint temperatures, 6°C, 14.5°C, 30°C, and 45°C. At 6°C the sample is assumed to be solid and k_a is essentially constant. The scatter in the 6°C data is not significantly greater than at most other temperatures but seems large because of the scale and small slope. A larger viscosity at 14.5°C than at 30°C is the probable cause of the smaller k_as at 14.5°C. The small positive slope of the 45°C data suggest the mechanism for the instability seen in the isotropic produces

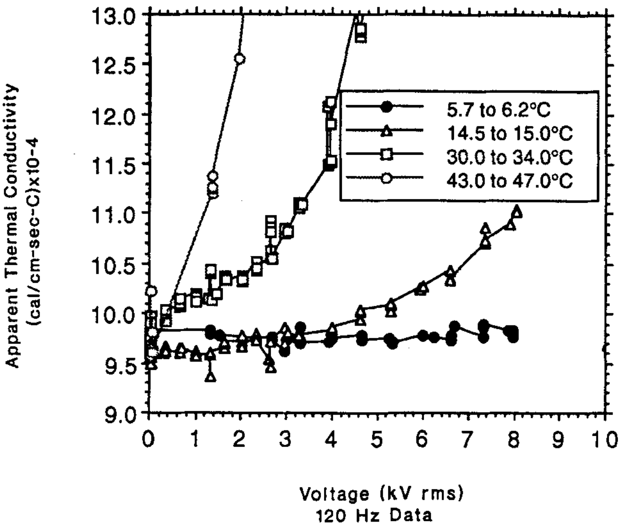

FIGURE 15 Variation of the apparent thermal conductivity k_a with rms voltage at a frequency of 120 Hz for the following phases/temperature-ranges: (1) Isotropic (43–47°C), (2) mid-nematic (30–34°C), (3) low-nematic (14.5–15°C), and (4) solid/crystalline (5.7–6.2°C). Pre-experiment DSC evaluation of the MBBA indicated $T_{K/N} = 21°C$ and $T_{N/I} = 40.5°C$. The variation in k_a is in large part due to the increase in viscosity with decreasing temperature, except for the data from the isotropic. There, loss of nematic ordering removes the anisotropic basis for the Carr-Helfrich mechanism.

a small but measurable enhancement of the thermal conductivity with increasing voltage.[9]

Figure 16 shows the behavior at 120 Hz of the internal heating Q_d associated with the values of k_a discussed above. The heating is expected to be dependent on viscosity since it arises from the frictional interaction between molecules.[16] The magnitude of the heating is temperature dependent at any field which is consistent with the viscosity being inversely related to temperature.[23] Note that the maximum Q_d (which still maintains a V^2 dependence) is observed when the MBBA is in the isotropic phase at the highest temperatures.

The next series of experiments were set-up to examine the behavior of k_a and Q_d near the nematic to isotropic transition. Since the temperature of the sample increased when a voltage was applied, the circulators were set such that the expected rise in sample temperature would take the sample into and out of the isotropic phase for a series of measurements. The amount of nematic order decreases significantly as the N/I transition is approached. However, the nematic order does not cease at the transition, but tails off in the isotropic (a post transitional effect). The magnitude of the EHD induced k_a is directly related to the amount of nematic order. Figure 17 depicts the behavior of k_a as the sample enters the isotropic and returns to the nematic and indicates a $T_{N/I}$ of about 39°C based on the behavior of k_a. The change in k_a is very abrupt from 5.2 kV_{rms} (36.9°C sample midpoint temperature) to 9.2 kV_{rms} (39.0°C). The increase of 2.1°C results in a change from 40×10^{-4} cal/cm-sec-°C to 11×10^{-4} cal/cm-sec-°C with ¾ of the change occurring in the first 0.7°C temperature increase.

Loss of nematic ordering destroys the Carr-Helfrich mechanism for separation of space charge normal to the applied field, and essentially eliminates the potential for EHD motion when the liquid crystal is in the isotropic phase. The occurrence

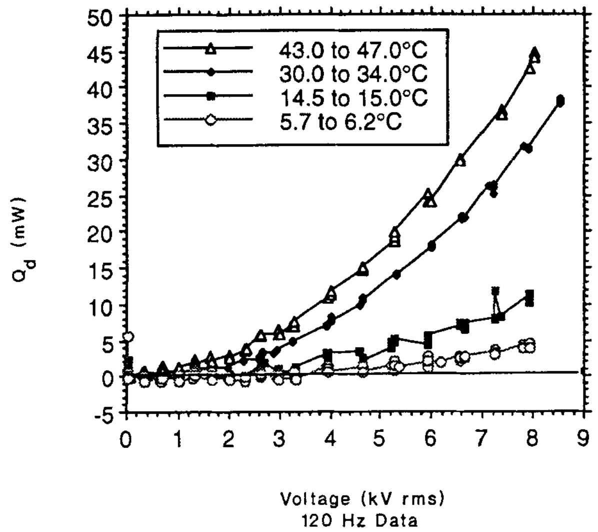

FIGURE 16 Variation of Q_d with voltage at 120 Hz for temperatures where the liquid crystal is in the isotropic (43–47°C), the mid-nematic (30–34°C), the low-nematic (14.5–15°C), and the solid/crystalline (5.7–6.2°C) phases.

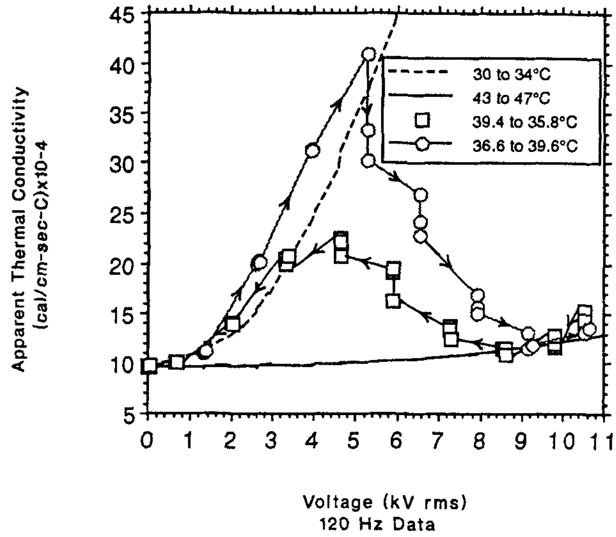

FIGURE 17 The variation of k_a about the nematic to isotropic transition point as a function of rms voltage at a frequency of 120 Hz. The dashed lines represent conditions where the MBBA sample was fully in the nematic (30–34°C). The solid line represents a range of temperatures within the isotropic (43–47°C). By increasing the voltage, internal heating within the sample was used to drive the sample into the isotropic (circles). Decreasing the voltage allowed the sample to return to the nematic (squares).

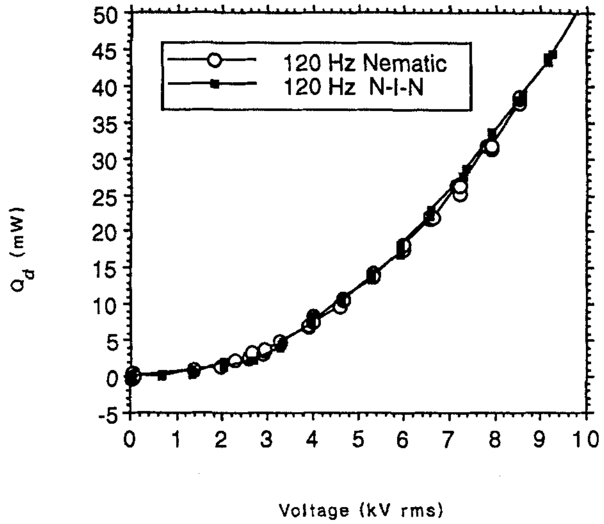

FIGURE 18 Variation of Q_d with voltage across the nematic to isotropic transition point. The circles represent data taken wholly in the nematic phase (32–34°C). The squares represent data taken when the liquid crystal was driven through the N-I-N transition. The data indicate that the heating is independent of the material anisotropy.

of a flow mechanism in which slow rolls persist into the isotropic is not unknown,[22] but detailed information concerning thick samples and Carr-Helfrich EHD motion is not available.

The linear correlation between k_a and Q_d established in the nematic is discontinued near the nematic-to-isotropic (N/I) transition. The factors causing the abrupt change in k_a seem to have no effect on Q_d. This is illustrated in Figure 18 where plots of Q_d as a function of rms voltage from data taken in the nematic is overlaid on similar plots data taken from the same set as Figure 17. The curves are essentially identical which suggests that all of the measured heat is associated with the Joule heating, and the frictional heat associated with the EHD motion is so small as to be unresolvable by this experiment.

5. CONCLUSIONS

The magnitude of the apparent thermal conductivity k_a in MBBA, shows a strong voltage, frequency, phase, and temperature/viscosity dependence. The increase in k_a with increasing voltage at a constant frequency, is largest when in the nematic phase and close to, but not within, the pretransitional effect range of the isotropic. Thus, k_a is largest for a constant frequency and voltage when the viscosity is lowest and nematic order is still maintained. When MBBA is in the nematic phase, the frequency at which k_a is at a maximum value increases with temperature. For example, the maximum value of k_a at 15.0°C occurs in the vicinity of 60 Hz, and the corresponding value at a temperature of 30°C occurs at approximately 129 Hz.

The apparent thermal conductivity of MBBA k_a does not vary with applied voltage when the liquid crystal is in the solid phase. Also, the measured values for k_a in the solid phase are larger than in the highest no-voltage values measured when the liquid crystal was in the nematic or isotropic phases.

Abrupt changes in k_a occur when MBBA undergoes a transition. First at the N/I transition, k_a decreases rapidly to a value approaching the k_0 (no-voltage) level due to the absence of the anisotropic material properties in the isotropic phase. However, k_a does not decrease all the way to the no-voltage k_0 level but persists in showing a small but positive increase with increasing voltage which may indicate a non-Carr-Helfrich driving mechanism. Secondly, at 24 Hz this MBBA sample exhibits a region of fluctuating flow alternating between seemly no-flow to high flow (high thermal conductivity) conditions. For a temperature of 15°C, this MBBA sample shows behavior consistent with a transition from the conduction regime (flow) into the dielectric regime (no-flow) with increasing frequency at a constant voltage. This frequency, like the cutoff frequency f_c of Williams domains, is expected vary in an inverse relationship with the resistivity ρ.

The existence of an "apparent" dielectric constant and resistivity, and the divergence thereof, plus the behavior of the power factor substantiate the existence of a voltage screening ionic double layer as described by Sprokel.[20] Ionic shielding is a maximum at DC, and becomes negligible for frequencies beyond 100 Hz. Calculations based on the magnitude of the internal heating indicates a resistivity ρ of about 5.7×10^9 Ohm-cm. This value may be too large due to the strong thermal coupling of the sample to the thermal shield and the corresponding thermal losses to the environment.

All of the measured or extrapolated data clearly indicate that the actual heat transport behavior of MBBA is a function of more than one variable. Ionic shielding, internal heating, viscosity changes with temperature, amount of nematic order, etc. all have significant effects. The data provides a general but detailed look at some of the multifaceted behavior of MBBA (specific ρ) under the influence of applied AC fields. The EHD behavior of MBBA with different resistivities is expected to show similar general trends but differ in details depending on the actual ρ. This study was intended to provide an initial but somewhat detailed look at the thermal transport properties of MBBA in the nematic phase.

Acknowledgment

This work was performed at the Naval Coastal Systems Center (Now Coastal Systems Station) in Panama City, Florida, under the sponsorship of the Office of Naval Technology (ONT). The work was executed under program NC3C, project number RP15S61. The authors gratefully acknowledge the individual insights and contributions of Drs. Girardeau Henderson and Robert McDonald and those of Messrs. George Allen, Dave Kendricks, Jimmy Barbee, Chuong Pham, William Hutt, and Karl Roeseberg.

References

1. E. Dubois-Violette, P. de Gennes and O. Parodi, *J. Physique*, **32**, 305 (1971).
2. P. Pieranski, E. Dubois-Violette and E. Guyon, *Phys. Rev. Lett.*, **30**, 736 (1973).
3. E. F. Carr, *Mol. Cryst. and Liq. Cryst.*, **7**, 253 (1969).
4. W. Helfrich, *J. Chem. Phys.*, **51**, 4092 (1969).
5. ORSAY Liquid Crystal Group, *Mol. Cryst. and Liq. Cryst.*, **12**, 251 (1971).
6. E. Bodenschatz, W. Zimmermann and L. Kramer, *J. Phys. France*, **49**, 1875 (1988).
7. J. H. Parker and E. F. Carr, *J. Chem. Phys.*, **55**, 1846 (1971).
8. K. Hirakawa and S. Kai, *Mol. Cryst. and Liq. Cryst.*, **40**, 261 (1977).
9. L. M. Blinov, *Electro-Optical and Magneto-Optical Properties of Liquid Crystals*, John Wiley and Sons, Inc. (1983).
10. P. Pieranski, F. Brochard and E. Guyon, *J. Physique*, **33**, 681 (1972).
11. D. H. Van Winkle, Unpublished Data, Williams domains form in thick MBBA cells (0.33 cm) after long time periods (hours) under a 10 volt 60 Hz field.
12. D. H. Van Winkle, J. Gurung and R. R. Biggers, "Electrodynamic Flow in Thick Liquid Crystal Cells," *Proc. Mat. Res. Soc. Symp.*, **177**, 311 (1990).
13. E. F. Carr, *Mol. Cryst. and Liq. Cryst.*, **111**, 161 (1984).
14. J. Hwalek and E. F. Carr, *J. Heat Trans. Eng.*, **8**, 36 (1987).
15. R. R. Biggers, J. Rish III and G. Henderson, "Influence of Electric Fields on Heat Transfer through Thermotropic Liquid Crystals," *Developments in Theoretical and Applied Mechanics Vol. 14, Proceedings of Fourteenth Southeastern Conference on Theoretical and Applied Mechanics*, 454 (1988).
16. *Electrical Engineers' Handbook*, 4th Ed., H. Pender and W. A. Del Mar, Eds., John Wiley and Sons, Inc., 18 (1949).
17. Holman, J. P., *Heat Transfer*, 4th Ed., McGraw-Hill, New York, NY, 1976.
18. Rule, D. L., private correspondence, Feb. 24, 1989.
19. Carr, E. F., private correspondence, Feb., 1988.
20. G. J. Sprokel, *Mol. Cryst. and Liq. Cryst.*, **22**, 249 (1973).
21. F. Rondelez, D. Diguet and G. Durand, *Mol. Cryst. and Liq. Cryst.*, **15**, 183 (1971).
22. A. Denat, B. Gosse and J. P. Gosse, *J. Chem. Phys.*, **2**, 319 (1973).
23. J. W. Summerford, J. R. Boyd and B. A. Lowry, *J. Appl. Phys.*, **46**, 970 (1975).